CMS Physics Analysis Summary

Contact: cms-pag-conveners-exotica@cern.ch 2017/07/06

Search for long-lived particles that stop in the CMS detector and decay to muons at $\sqrt{s} = 13$ TeV

The CMS Collaboration

Abstract

A search for long-lived particles that are produced in proton-proton collisions at the CERN LHC, come to rest in the CMS detector, and decay to muons is presented. The decays of stopped particles could be observed during the intervals between LHC beam crossings, at times well separated from any proton-proton collisions. The analysis uses 39 fb^{-1} of $\sqrt{s} = 13$ TeV data collected by CMS in 2015 and 2016, during a search interval totaling 744 hours of trigger livetime. The results are interpreted with one model that predicts a long-lived gluino and another model that predicts a long-lived particle that has twice the electron charge and that behaves like a lepton. Cross section limits are set as a function of lifetime and as a function of mass, for lifetimes between 100 ns and 10 days. This is the first search for stopped particles that decay to muons at the LHC.

1 Introduction

Massive, long-lived particles (LLPs) do not exist in the standard model (SM). Therefore, any sign of them would be an indication of new physics. There are many extensions of the SM that predict LLPs [1–6]. We currently have no explanation of the dark matter observed in the universe. We have yet to find dark matter, which could be a neutral, stable particle beyond the SM. Furthermore, cosmology may hint that a charged, LLP could exist, although it rules out absolutely stable charged massive particles, as they would be observable today [7–9]. Our present model of big bang nucleosynthesis (BBN) has difficulties in explaining the observed lithium production, but a charged LLP that decays during or after the time of BBN could resolve this disagreement [10].

LLPs could be sufficiently massive that they might lose enough energy through ionization or hadronization, depending on the type of particle, to come to rest inside the detector material [11]. If the LLP is colored, it will hadronize prior to traversing the detector, creating a R-hadron, which will eventually stop in the detector [12–16]. These stopped particles or R-hadrons could then decay seconds, days, or weeks after the proton-proton collision. These decays could occur when there are no collisions and the detector is relatively quiet; the observation of such decays would be a clear sign of new physics. If the stopped particles decay to muons, the major background to such a search would be cosmic rays that survive the 100 m trip through the earth to the CMS detector. Furthermore, decays to leptons are key flags of heavy particle production, and the presence of leptons that are delayed with respect to the collision may signal new physics.

We present here the first search at the LHC for LLPs that come to a stop in the detector and decay to muons some time after the pp collision in which they were produced. Previous CMS and ATLAS analyses have searched for stopped R-hadrons by looking for calorimeter deposits during gaps between LHC beam crossings [17–20]. The most restrictive of these is from CMS, using $18.6\,\text{fb}^{-1}$ of 8 TeV data, corresponding to 281 hours of trigger livetime, which excludes long-lived gluinos with masses below 1000 GeV and long-lived top squarks with masses below 525 GeV [19]. These searches are complimentary to other searches for heavy stable charged particles (HSCPs) that pass through the detector and can be identified by their energy loss and time-of-flight information [21–35]. The HSCP limits will be discussed below, when the relevant models are described.

We select events with a custom trigger designed to record events that are out-of-time with collisions. Then, we apply offline criteria to reject muon system noise, beam halo, and cosmic muons. After these criteria are applied, the only non-negligible background that survives comes from cosmic muons. We model this cosmic muon background with data, and estimate its contribution by extrapolating from a background-dominated region to the signal region. Finally, we determine the number of observed events and the number of predicted background events that escape our offline selection criteria.

2 The CMS Detector

The central feature of the CMS apparatus is a superconducting solenoid of 6 m internal diameter, providing a magnetic field of 3.8 T. Within the superconducting solenoid volume are a silicon pixel and strip tracker, a lead tungstate crystal electromagnetic calorimeter (ECAL), and a brass and scintillator hadron calorimeter (HCAL), each composed of a barrel and two endcap sections. Forward calorimeters extend the pseudorapidity coverage provided by the barrel and endcap detectors. Muons are measured in gas-ionization detectors embedded in the

steel flux-return yoke outside the solenoid. Muons are measured in the pseudorapidity range $|\eta| < 2.4$, with detection planes made using three technologies: drift tubes (DTs) in the barrel, cathode strip chambers (CSCs) in the endcaps, and resistive plate chambers (RPCs) in both the barrel and the endcaps. All these technologies provide both position and timing information. The first level (L1) of the CMS trigger system, composed of custom hardware processors, uses information from the calorimeters and muon detectors to select the most interesting events in a fixed time interval of less than 4 μs. The high-level trigger (HLT) processor farm further decreases the event rate from around 100 kHz to less than 1 kHz, before data storage. A more detailed description of the CMS detector, together with a definition of the coordinate system used and the relevant kinematic variables, can be found in Ref. [36].

3 Data and Monte Carlo Simulation Samples

This search is performed with 2.8 fb^{-1} (during 2015) and 36.2 fb^{-1} (during 2016) of 13 TeV data. The data were collected with a custom trigger, which selects events based on at least one muon detected with muon system measurements that is separated by at least 50 ns from the pp collision time. The trigger selected events containing muons with a transverse momentum p_{T} of at least 35 (40) GeV during the entire 2015 (2016) run. This corresponds to 155 and 589 hours of trigger livetime, that is, the amount of time our trigger is live in between collisions, in 2015 and 2016, respectively.

We also use a sample of cosmic ray data from dedicated cosmic runs taken during 2016, when there are no LHC beams, which we call "cosmic muon data" below. The data were collected with the same custom triggers described above. These data were used to determine how the background from cosmic rays would appear in the detector, and in particular, they were used to evaluate some systematic uncertainties (see Section 7). However, they were not actually used in the background prediction (see Section 6).

Long-lived gluinos can arise in the context of Split SUSY [37, 38]. Split SUSY is a model in which SUSY is broken near the unification scale. This results in the supersymmetric squarks and sleptons being very heavy ($>$ 1 TeV), while the gauginos remain relatively light and account for the unification of the gauge couplings. The gluino is the only colored particle at this low mass scale, so it can only decay through t-channel exchanges of a virtual squark. Since the squarks are very massive, this decay will be suppressed and thus, the gluino can have a long lifetime, possibly up to 100 s. Gluinos are pair produced, and they would form R-hadrons in the detector, interacting via the strong force and hadronizing with quarks. The gluino could have a three-body decay, which is referred to in Ref. [39] as the "T3lh" simplified model [40, 41]. The gluino decays to a quark-antiquark pair and a NLSP neutralino ($\tilde{g} \to q\bar{q}\tilde{\chi}_2^0$). Then the NLSP neutralino decays to a pair of oppositely-signed muons, and the LSP neutralino ($\tilde{\chi}_2^0 \to \mu^+\mu^-\tilde{\chi}_{LSP}^0$). The mass of the LSP neutralino was chosen to be 1/4 of the gluino mass, and the mass of the NLSP neutralino was chosen to be 2.5 times the LSP neutralino mass.

Multiply charged massive particles (mchamps) arise from modified Drell-Yan production of long-lived lepton-like fermions. In this scenario, new massive spin-1/2 particles have arbitrary electric charge and are neutral under SU(3)$_C$ and SU(2)$_L$, and therefore couple only to the photon and the Z boson [42]. There are several BSM theories that give rise to particles with charge Q not equal to e, namely mchamps or fractionally charged massive particles (fchamps) [42]. The most restrictive limits on HSCP mchamps with $|Q| = 2e$ exclude masses below 890 GeV [35]. We assume the mchamps with $|Q| = 2e$ behave like doubly charged Higgs particles ($\mathrm{H}^{\pm\pm}$) and can directly decay to two muons each [43]. The two muons from the stopped mchamp decay

will be back-to-back.

There are three major steps in the signal generation process. In Stage 1, a LLP is generated with PYTHIA [44, 45] and propagated through the detector with GEANT4 v9.2 [46, 47] for each signal. Some fraction of these are sufficiently slow-moving to come to a stop in the detector material. Thus, the Stage 1 simulation determines the LLP's stopping efficiency. For the strongly interacting LLPs, the hadronization is done via the PYRAD subroutine, resulting in the R-hadron. The fraction of produced R-hadrons that contain a gluino and a valence gluon is set to 10%. Then, in Stage 2, the parent LLP or R-hadron is forced to decay at the stopping position defined in Stage 1 (via appropriate channels) to muons, which are propagated through the detector. Thus, Stage 2 determines the reconstruction efficiency. Finally, Stage 3 is a pseudo-experiment Monte Carlo (MC) simulation used to estimate the probability for stopped particle decays to occur when the detector is on but there are no collisions occurring. The Stage 3 MC simulation determines an effective luminosity by using the good data-taking periods and the LHC filling scheme to calculate the fraction of stopped particle decays that occur when the trigger is live. The effective luminosity for a given particle lifetime is defined as the integrated luminosity multiplied by the probability that the particle decays at a time when the trigger is live in between collisions. In other words, the Stage 1 and 2 MC simulation determine how the signal will look in the detector, and Stage 3 determines when it will occur.

It is possible for one or two LLPs per interaction to stop in the detector, since for each signal, the LLP is pair produced. If there is more than one stopped particle per interaction, it is unlikely that they both will stop and decay close in time with each other, if the lifetime of the stopped particle is long. Given that the time window associated with a triggered event is on the order of 100 ns, and the lifetimes this analysis is sensitive to are longer than that, we will assume that every decay of a stopped particle is triggered separately. In other words, the decay of each stopped particle will be in a separate event. Therefore, in the Stage 2 MC simulation, if a second particle is stopped in the detector, the additional particle's decay is put in a new event. This assumption has a negligible effect on the analysis sensitivity for the lifetimes considered in this analysis.

The likelihood that a LLP will stop in the detector is calculated by the Stage 1 MC simulation. Figure 1 shows the stopping efficiency as a function of mass for gluinos and mchamps. The mchamps have the highest stopping probability because they have twice the electron charge. The R-hadrons from the gluinos are the next most likely to stop in the detector, as they can be either singly or doubly charged.

4 Analysis Strategy and Techniques

To search for stopped LLPs that decay to muons, we trigger on muons that are out-of-time with respect to the collision. We model the signal with a MC simulation of LLPs that are stopped throughout the detector and decay to muons. We identify background sources: muons from cosmic rays, muon system noise, and beam halo. The cosmic muons are modeled with data and studied carefully, while noise and beam halo backgrounds are negligible after the full selection criteria and can be ignored. We use the muon time-of-flight (TOF) information from the DTs and RPCs to distinguish the background cosmic muons from signal. These key variables are described below.

A new muon reconstruction algorithm was developed for this analysis called displaced standalone (DSA) muon tracks [48]. The DSA tracks are reconstructed using only hits in the muon chambers, and they have no constraints to the beam spot. The DSA track reconstruction effi-

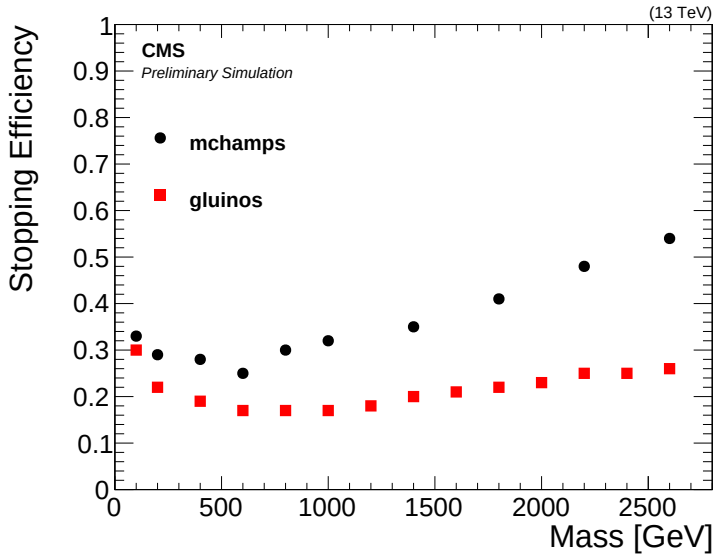

Figure 1: The stopping efficiency per particle as a function of mass for gluinos and mchamps. The mchamps have $|Q| = 2e$.

ciency is taken from the simulation.

In the pairs of figures below depicting DSA muon track variables (Figs. 3, 5, and 7), we show the upper hemisphere DSA muon tracks on the left, meaning tracks reconstructed in upper half of the detector, and the lower hemisphere DSA muon tracks on the right, meaning tracks reconstructed in the lower half of the detector. The usefulness of splitting the data this way will become clear below.

Furthermore, we will present histograms and tables that show only the 2016 data and results, since the 2015 data look similar and gives a marginal increase in sensitivity. The limits will be presented for the combination of 2015 and 2016 data.

Timing information in the DTs and RPCs can be used to distinguish muons from the signal from the cosmic muon background because the timing information can provide the direction of the muon, namely, whether it is incoming toward the detector center or outgoing away from the detector center. Cosmic muons will predominantly be incoming when traversing the upper hemisphere and outgoing when traversing the lower hemisphere, as they come in from the top of the detector and continue to move downwards. Muons from the signal, on the other hand, will be outgoing in both hemispheres.

We first consider several time-of-flight variables from the DTs, where an accurate measurement of the time-of-flight can be obtained.

t_{DT} is the time at the point of closest approach to the interaction point (IP) as measured by the DTs, assuming the muon is outgoing. Since cosmic muons are incoming in the upper hemisphere and outgoing in the lower hemisphere, t_{DT} of the upper and lower hemisphere cosmic muons will be about 40 to 50 ns apart. Also, since cosmic muons do not arrive in sync with the LHC collision clock, the reconstructed time assigned to them depends on how a given event was triggered. If the cosmic muon traversing the upper hemisphere triggers the event, which happens about 90% of the time, this DSA muon track will have t_{DT} around 0 ns, and the accompanying lower hemisphere muon will have t_{DT} of about +50ns. About 10% of the time the lower hemisphere cosmic muon triggers the event, in which case it will have t_{DT} of about 0 ns, and then the preceding upper hemisphere cosmic muon will be reconstructed with t_{DT} of about

-50 ns. On the other hand, muons from the signal will both be outgoing, so they are usually both reconstructed with t_{DT} of about 0 ns. See Fig. 2 for a schematic diagram of t_{DT} for cosmic muons and muons from the signal.

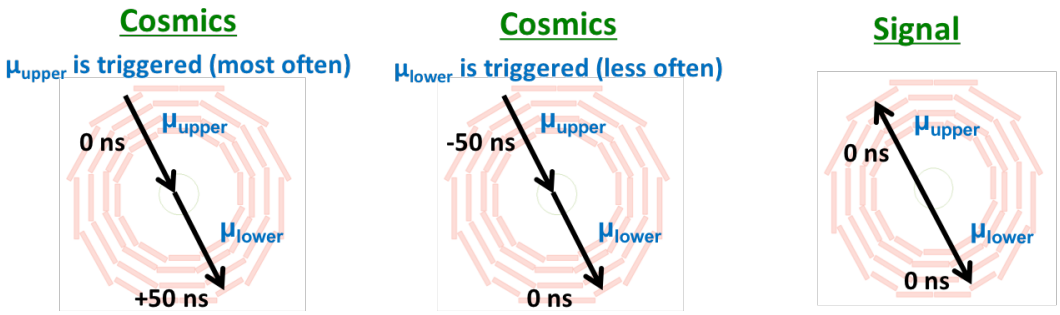

Figure 2: A diagram showing the typical direction and the corresponding t_{DT} values of muons coming from cosmic muon background (left) and signal (right). This is a simple schematic and does not necessarily reflect how close the muons would come to the beamspot. Furthermore, the muons from the signal are not necessarily back-to-back.

Figure 3 shows the distribution of t_{DT} for the upper and lower hemisphere DSA muon tracks. In the cosmic muon dominated data t_{DT} distributions, the major peaks are when the upper hemisphere DSA muon track is found at a time of about 0 ns, and when the lower hemisphere DSA muon track is found at about 50 ns. As explained above, this corresponds to the situation when the upper hemisphere muon is triggered, and thus given a time of about 0 ns, and the lower hemisphere muon arrives about 50 ns later.

The two early shoulders in the data t_{DT} distributions, at about -50 ns for the upper hemisphere DSA muon track and at about 0 ns for the lower hemisphere DSA muon track, can be explained by a lower hemisphere DSA muon track being triggered when the upper hemisphere muon was missed by the trigger. Thus, the time of the lower hemisphere DSA muon track is about 0 ns. Since this variable shows the offline reconstruction, we can see that offline, the missing upper hemisphere muon was recovered, and it was found about 50 ns earlier than the lower hemisphere muon, that is, at about -50 ns. This scenario is not modeled in the cosmic muon simulation.

Another DT timing variable that is used is β^{-1}, which is defined as the speed of light divided by the velocity (c/v) and is therefore directly proportional to the TOF. We determine β^{-1} from the slope of a straight line fit to the times and the distances from the IP of the DT hits, without a constraint to the beam spot.

β^{-1} gives us the direction of the muon, that is, whether it is incoming toward the beam spot or outgoing from the beam spot. Outgoing muons should have a positive β^{-1} and incoming muons should have a negative β^{-1}. As a result, this β^{-1} measurement can distinguish the cosmic muon background from the muons from the signal in the upper hemisphere. See Fig. 4 for a schematic diagram of β^{-1} for cosmic muons and muons from the signal. Cosmic muons will predominantly be incoming in the upper hemisphere and outgoing in the lower hemisphere, as they come in from the top of the detector and continue to move downwards. The signal, on the other hand, will be outgoing in both hemispheres.

β^{-1} is plotted in Fig. 5. Cosmic muons are peaked at $\beta^{-1} = -1$ when the incoming muon is in the upper hemisphere and at $\beta^{-1} = +1$ when the outgoing muon in the lower hemisphere. The β^{-1} distribution for cosmic muons is simpler than t_{DT} distribution because the details about which muon is triggered are no longer relevant: only the direction of the muons matters.

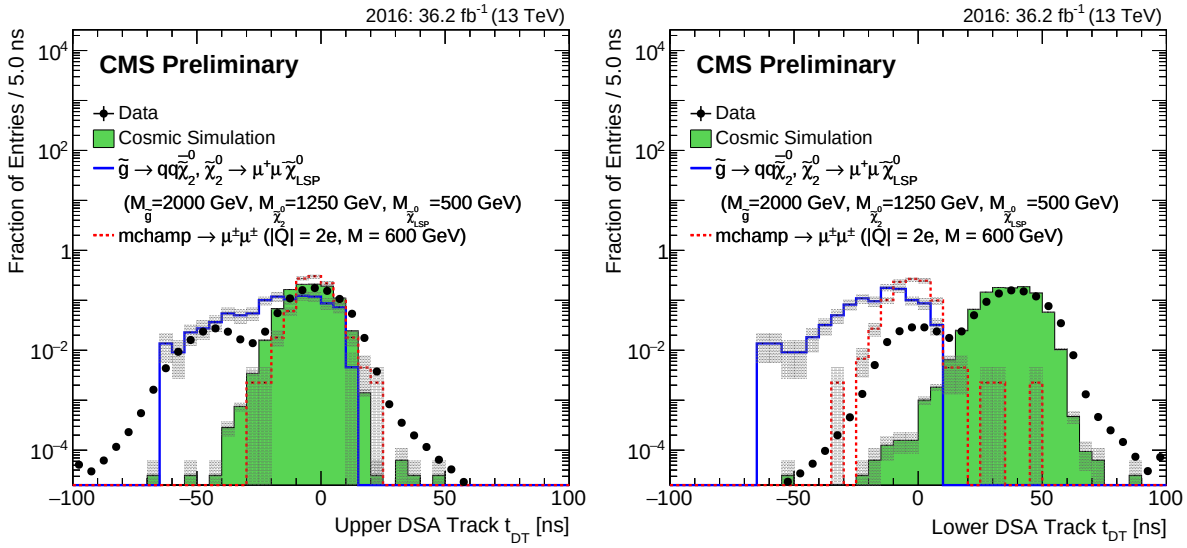

Figure 3: DSA muon track t_{DT} for 2016 search sample data, cosmic muon MC simulation, 2000 GeV gluinos, and 600 GeV mchamps. t_{DT} of the upper (left) and lower (right) hemisphere DSA tracks is plotted. The events plotted pass a subset of the full analysis selection that is designed to select good quality DSA muon tracks but does not reject the cosmic muon background (see Section 5). The gluino and mchamp distributions are not exactly the same because the two muons from the mchamp decay are back-to-back, but the two muons from the gluino decay are not. The grey bands indicate the statistical uncertainty in the simulation. The histograms are normalized to unit area.

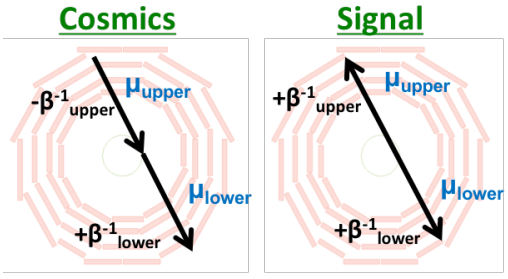

Figure 4: A diagram showing the typical direction and thus, the sign of β of muons coming from cosmic muon background (left) and signal (right). This is a simple schematic and does not necessarily reflect how close the muons would come to the beamspot. Furthermore, the muons from the signal are not necessarily back-to-back.

Muons from the signal have only one peak at a β^{-1} value of +1, as these muons are always outgoing.

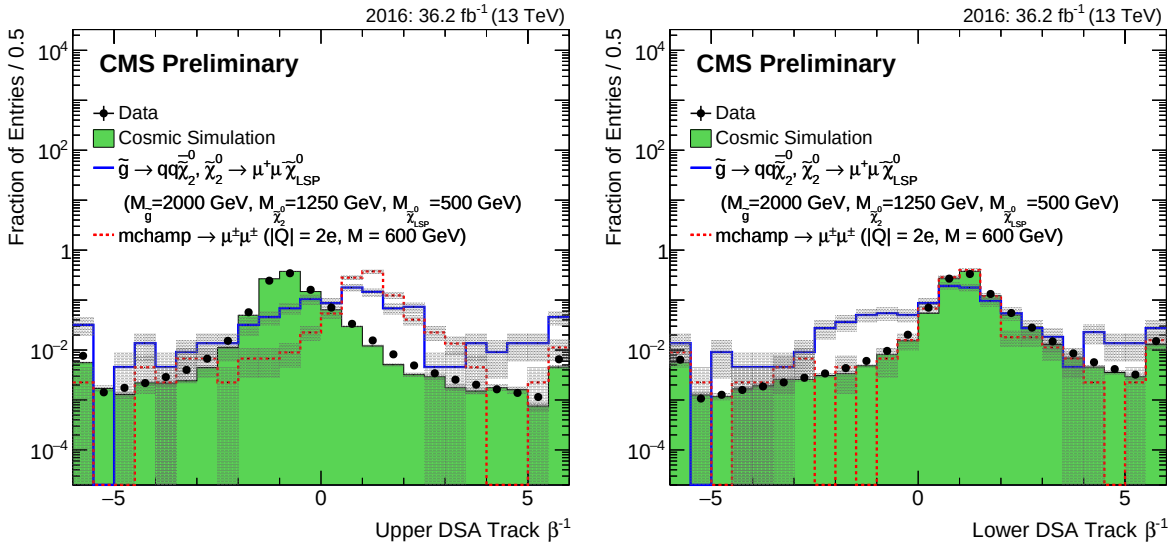

Figure 5: DSA muon track β^{-1} for 2016 search sample data, cosmic muon MC simulation, 2000 GeV gluinos, and 600 GeV mchamps. The β^{-1} of the upper (left) and lower (right) hemisphere DSA tracks is plotted. The events plotted pass a subset of the full analysis selection that is designed to select good quality DSA muon tracks but does not reject the cosmic muon background (see Section 5). The grey bands indicate the statistical uncertainty in the simulation. The histograms are normalized to unit area.

In addition to these two variables, we use a timing measurement from the RPCs that assigns a bunch crossing (BX) to each hit. For each of the six layers of the RPCs, the hit is given a BX assignment. A typical prompt muon created at the IP will have each of its RPC BX assignments be zero; thus, its RPC BX pattern will be 0,0,0,0,0,0, if all the RPC layers gave good BX measurements. The BX assignments of cosmic muons are especially useful in the lower hemisphere of the detector, as the incoming cosmic muons will typically trigger the event and thus be assigned BX values of zero in each RPC layer, but the outgoing cosmic muons will often be assigned positive BX values. For example, a typical lower hemisphere cosmic muon BX pattern will be 2,2,2,2,2,2 for the RPC layers with good timing measurements, ranging from the innermost to the outermost. For our signal, the RPC BX assignments for each muon will typically each be zero. See Fig. 6 for a schematic diagram of the BX assignments for cosmic muons and muons from the signal.

Given the BX assignments in each RPC layer for a muon, we can compute the average RPC hit BX assignment multiplied by 25 ns as the RPC time for a track (t_{RPC}) and use this as a discriminating variable. See Fig. 7 for the distribution of t_{RPC} in signal and background. The typical muon from signal will have an t_{RPC} of 0 ns for both upper and lower hemisphere DSA muon tracks. On the other hand, a cosmic muon will typically have a lower hemisphere t_{RPC} of 25 or 50 ns and an upper hemisphere t_{RPC} of 0 ns.

We can further exploit the TOF variables if we examine muons in the upper hemisphere and lower hemisphere separately and devise TOF variables that are the difference between that of the upper hemisphere muon and that of the lower hemisphere muon. These Δ TOF variables are better at distinguishing between signal and background than if the upper and lower hemisphere muons are treated independently. Furthermore, the Δ TOF variables have better data to cosmic background MC simulation agreement than that of the individual upper and lower

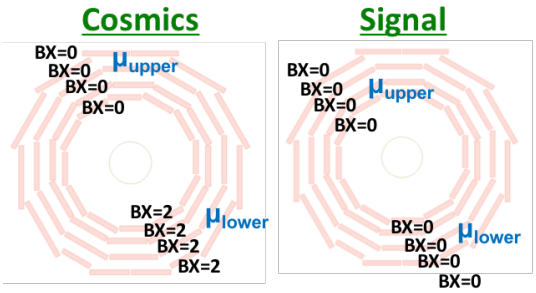

Figure 6: A diagram showing the typical RPC BX assignments of muons coming from cosmic muon background (left) and signal (right). This is a simple schematic and does not necessarily reflect how close the muons would come to the beamspot. Furthermore, the muons from the signal are not necessarily back-to-back.

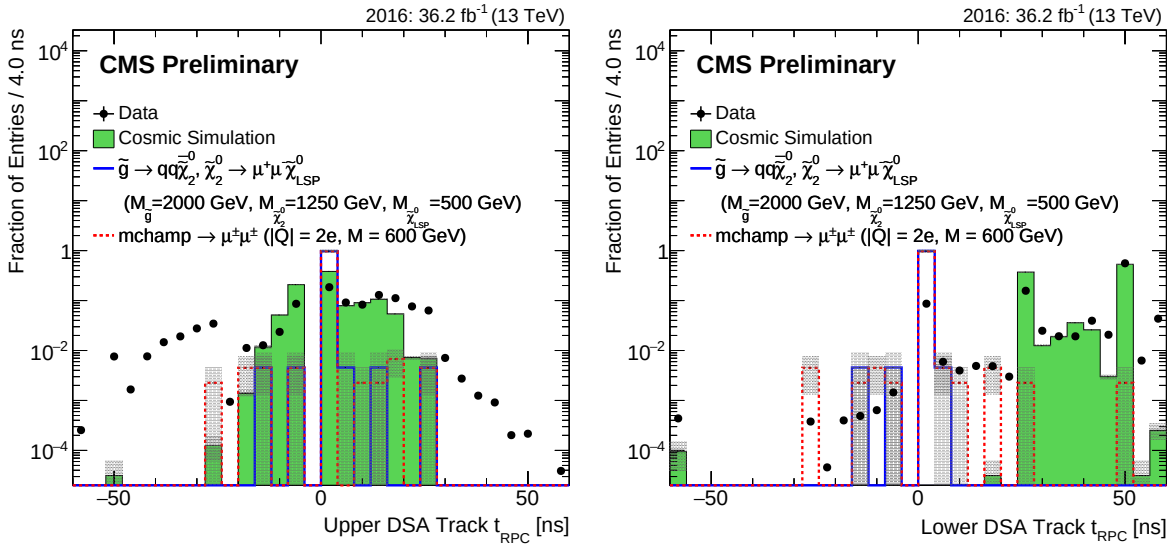

Figure 7: DSA muon track t_{RPC} for 2016 search sample data, cosmic muon MC simulation, 2000 GeV gluinos, and 600 GeV mchamps. t_{RPC} of the upper (left) and lower (right) hemisphere DSA tracks is plotted. The events plotted pass a subset of the full analysis selection that is designed to select good quality DSA muon tracks but does not reject the cosmic muon background (see Section 5). The grey bands indicate the statistical uncertainty in the simulation. The histograms are normalized to unit area.

hemisphere TOF variables. As will be seen below, the Δ TOF variables, and not the individual upper and lower hemisphere TOF variables, are used in the analysis.

We define the Δ TOF variables as the TOF variable of the upper hemisphere muon minus that of the lower hemisphere muon:

$$\Delta t_{\mathrm{DT}} = t_{\mathrm{DT}}(\mathrm{upper}) - t_{\mathrm{DT}}(\mathrm{lower}) \quad (1)$$

$$\Delta t_{\mathrm{RPC}} = t_{\mathrm{RPC}}(\mathrm{upper}) - t_{\mathrm{RPC}}(\mathrm{lower}) \quad (2)$$

These Δ TOF variables are plotted in Fig. 8. In these plots, the cosmic muons have a large negative time because the upper hemisphere time is less than the lower hemisphere time. Conversely, the muons from the signal have a time around 0 ns in these plots because the two muons are both outgoing and reconstructed to have similar times as measured at the IP.

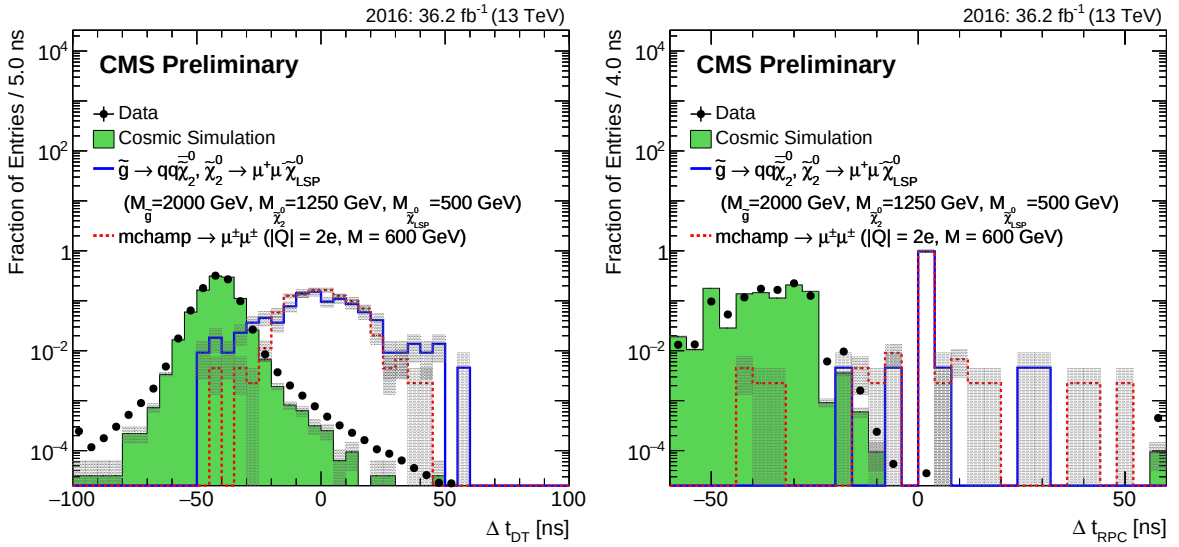

Figure 8: DSA muon track Δt_{DT} (left) and Δt_{RPC} (right) for 2016 search sample data, cosmic muon MC simulation, 2000 GeV gluinos, and 600 GeV mchamps. The events plotted pass a subset of the full analysis selection that is designed to select good quality DSA muon tracks but does not reject the cosmic muon background (see Section 5). The grey bands indicate the statistical uncertainty in the simulation. The histograms are normalized to unit area.

5 Event Selection

The LLP generated by the signal MC simulation is required to stop in the detector.

The data and MC simulation events must pass the trigger and have zero reconstructed vertices. We place selection criteria to require good quality DSA tracks. Specifically, we require that there are exactly one good DSA track in the upper hemisphere and exactly one good DSA track in the lower hemisphere. Both DSA tracks must have p_{T} greater than 50 GeV, at least three DT chambers with valid hits, and at least three valid RPC hits. The DSA tracks must also have zero valid CSC hits, and in this way, we select tracks in the CMS barrel and reduce the background from beam halo.

We also place selection criteria on both the upper and lower hemisphere DSA tracks in order to obtain a good time measurement, and then we ask for the time measurement to be signal-like. We require at least eight DT hits with good timing measurements per DSA track. We

require that the uncertainty in the time measured at the IP for DSA tracks, assuming the muon is outgoing, is less than 5.0 ns. We require that the β^{-1} of the lower hemisphere DSA track is greater than 0, to ensure that there are no upwards traveling cosmic muons and to reduce beam halo. Lastly, we require that the Δt_{DT} is greater than -20 ns and that the Δt_{RPC} is greater than -7.5 ns, which greatly reduces the cosmic muon background.

Figs. 3, 5, 7, and 8 show events that pass a subset of the selection criteria described above, which was designed to select good quality DSA muon tracks but is dominated by the cosmic muon background. This selection is defined by the same trigger and reconstructed vertices requirements as above, and also exactly one DSA track in the upper hemisphere and exactly one DSA track in the lower hemisphere. Looser requirements are placed on the DSA track p_{T} (greater than 10 GeV), the number of DT chambers with valid hits (greater than one), and the number of valid RPC hits (greater than one). We make the same requirements on the number of DT hits with good timing measurements per DSA track and the number of valid CSC hits as above for this selection. None of the remaining criteria above are repeated here.

All of these selection criteria were developed while the analysis was blinded, meaning that we did not look at the data in the signal region, which is defined by $\Delta t_{\mathrm{RPC}} > -7.5$ ns.

6 Background Modeling

The background is estimated by extrapolating the data from a background-dominated region into the signal region. We apply the full event selection to the data except the Δt_{DT} criterium, and we invert the Δt_{RPC} criterium. We then fit the Δt_{DT} distribution with the sum of two Gaussian distributions and a Crystal Ball function. Next, we compute the integral under the fit, when $\Delta t_{\mathrm{DT}} > -20$ ns. Then, we tighten the lower selection criteria on Δt_{RPC} to -50 ns $< \Delta t_{\mathrm{RPC}} < -7.5$ ns, then -45 ns $< \Delta t_{\mathrm{RPC}} < -7.5$ ns, etc. in steps of 5 ns up to -10 ns $< \Delta t_{\mathrm{RPC}} < -7.5$ ns. For each Δt_{RPC} selection step, we again compute the integral under the fit when $\Delta t_{\mathrm{DT}} > -20$ ns. Finally, we plot each integral under the fit when $\Delta t_{\mathrm{DT}} > -20$ ns as a function of the lower selection on Δt_{RPC}, and fit this with the error function to extrapolate to when $\Delta t_{\mathrm{RPC}} > -7.5$ ns (see Fig. 9). Given this extrapolation, we predict 0.04 ± 0.00 background events in 2015 data and 0.50 ± 0.02 background events in 2016 data. The statistical uncertainty in the background prediction is from the uncertainty in the error function fit parameters.

The systematic uncertainty in the background prediction is evaluated by repeating the steps above, except changing the fit of the Δt_{DT} distribution to the sum of two Gaussian distributions and a Landau function. Using the error function fits to extrapolate to $\Delta t_{\mathrm{RPC}} > -7.5$ ns gives a prediction of 0.07 ± 0.06 background events in 2015 data and 0.10 ± 0.01 background events in 2016 data. Thus, the background prediction is: 0.04 ± 0.00(stat)$\pm$0.03(syst) background events in 2015 data and 0.50 ± 0.02(stat)$\pm$0.40(syst) background events in 2016 data.

Despite the fact that we require exactly one upper hemisphere DSA track and exactly one lower hemisphere DSA track, there could still be some background from two coincident cosmic muons. This background from two coincident cosmic muons could occur if the upper DSA track of one cosmic muon is reconstructed and if the lower hemisphere DSA track of the other is also reconstructed. We have estimated this contribution from data and found it to be negligible.

7 Systematic Uncertainties

The luminosity is estimated within 2.3% in 2015 [49] and 2.5% in 2016 [50].

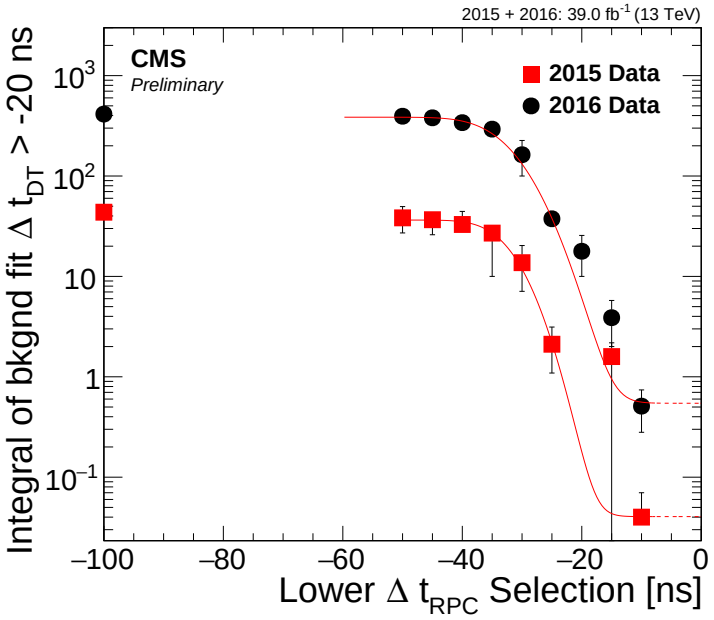

Figure 9: The integral under the fit to Δt_{DT} with the sum of two Gaussian distributions and a Crystal Ball function, when $\Delta t_{\mathrm{DT}} > -20$ ns, as a function of the lower Δt_{RPC} selection, for 2015 (red squares) and 2016 (black circles) data. The points are fitted with an error function, and used to extrapolate to the signal region, which is defined as $\Delta t_{\mathrm{RPC}} > -7.5$ ns.

We considered the systematic uncertainty associated with the MC simulation modeling of the Q/p_{T} resolution by comparing this resolution in cosmic muon data and cosmic muon MC simulation. The resolution studied compares the charge divided by the p_{T} (that is, Q/p_{T}) of the upper and lower hemisphere muons:

$$R(Q/p_{\mathrm{T}}) = \frac{(Q/p_{\mathrm{T}})^{\mathrm{upper}} - (Q/p_{\mathrm{T}})^{\mathrm{lower}}}{\sqrt{2}(Q/p_{\mathrm{T}})^{\mathrm{lower}}} \tag{3}$$

Then we plotted the standard deviation of Gaussian fits of the resolution, as a function of the reference lower hemisphere p_{T}, for cosmic muon data and cosmic muon MC simulation. A fit of the ratio between data and MC simulation in this plot for lower hemisphere $p_{\mathrm{T}} > 50\,\mathrm{GeV}$ gives a difference between cosmic muon data and cosmic muon MC simulation of 9.0% (5.3%) in the 2015 (2016) analysis. We then propagated this resolution uncertainty to an uncertainty in the signal efficiency by smearing the momentum distribution of muons in the signal and observing the corresponding variation in the signal yields. We take the largest variation in the signal yield, namely, 13% (7%) in the 2015 (2016) analysis, as the systematic uncertainty in the modeling of the Q/p_{T} resolution.

There can also be a systematic uncertainty associated with the trigger acceptance. Since the largest difference between data and MC simulation in the plateau of the trigger turn-on curves is 13% (2.8%) in the 2015 (2016) analysis, we take these values as the systematic uncertainty in the trigger acceptance.

In obtaining constraints on a particular model, substantial uncertainties arise since the signal yield is sensitive to the stopping probability. While the GEANT4 simulation used to derive the stopping probability very accurately models both the electromagnetic and nuclear interaction energy-loss mechanisms, the relative contributions of these energy-loss mechanisms to the stopping probability depends significantly on unknown R-hadron spectroscopy. We do not

consider this dependence to be a source of error, however, since given a particular model for the spectrum, the resultant uncertainty in the stopping probability is small.

The systematic uncertainties described above are all applied to the signal MC simulation. The systematic uncertainties in the signal efficiency are summarized in Table 1. The background method systematic uncertainty was described above.

Table 1: Systematic uncertainties in the signal efficiency for the 2015 and 2016 analyses.

Systematic Uncertainty	2015	2016
Luminosity	2.3%	2.5%
Q/p_{T} Resolution Mis-modeling	13%	7%
Trigger Acceptance	13%	2.8%

8 Results

We predict $0.04 \pm 0.00(\mathrm{stat}) \pm 0.03(\mathrm{syst})$ background events in 2015 and $0.50 \pm 0.02(\mathrm{stat}) \pm 0.40(\mathrm{syst})$ background events in 2016. There are zero observed events in both 2015 and 2016 data that pass all of the selection criteria.

Tables 2 and 3 show the signal stopping and reconstruction efficiency for each signal mass. The reconstruction efficiency is the efficiency of an event to pass all of the selection criteria, including the trigger, and it is computed independently of the stopping efficiency. This reconstruction efficiency also includes the correction needed for the trigger acceptance (see the discussion in Section 7 above). We lose signal efficiency because the ability to trigger on a muon is somewhat biased toward the beam spot, although the muons from our signal can be very displaced. Furthermore, we lose signal efficiency because we need a very good quality DSA muon track with a long lever arm and a good timing measurement. In addition, we lose geometrical acceptance when we require exactly one DSA track traversing the upper hemisphere and exactly one DSA track traversing the lower hemisphere, particularly for the gluino decay, which does not produce back-to-back muons, unlike the mchamp decay. The numbers in these tables represent the maximum signal that can be measured before considering the lifetime of the stopped particle.

Table 2: Gluino stopping efficiency, reconstruction efficiency, and the number of expected gluino events with lifetimes between 10 μs and 1000 s assuming 100% BF, for each mass for the 2016 analysis.

Gluino Mass [GeV]	Gluino Stopping Efficiency	Gluino Reconstruction Efficiency	Expected Gluino Events
400	0.19	0.0015	370
600	0.17	0.0024	51
800	0.17	0.0037	12
1000	0.17	0.0029	2.2
1200	0.18	0.0025	0.52
1400	0.20	0.0031	0.21
1600	0.21	0.0029	0.067
1800	0.22	0.0023	0.019
2000	0.23	0.0020	0.0062
2200	0.25	0.0028	0.0035
2400	0.25	0.0025	0.0012
2600	0.26	0.0025	0.00045

Table 3: Mchamp stopping efficiency, reconstruction efficiency, and the number of expected mchamp events with lifetimes between 10 μs and 1000 s assuming 100% BF, for each mass for the 2016 analysis.

Mchamp Mass [GeV]	Mchamp Stopping Efficiency	Mchamp Reconstruction Efficiency	Expected Mchamp Events
100	0.33	0.0059	100
200	0.29	0.041	48
400	0.28	0.045	3.9
600	0.25	0.042	0.49
800	0.30	0.038	0.12
1000	0.32	0.035	0.036
1400	0.35	0.032	0.0041
1800	0.41	0.027	0.00060
2200	0.48	0.026	0.000097
2600	0.54	0.026	0.000014

We were sensitive to 155 (589) hours of trigger livetime during the 2015 (2016) run, as determined by the pseudo-experiment Stage 3 MC simulation. The maximum effective luminosity is about 1.4 (13.7) fb^{-1}, which is reasonable when considering the integrated luminosity of 2.8 (36.2) fb^{-1} and the fact that the trigger is live 32% (37%) of the orbit for the most common bunch spacing in 2015 (2016).

We perform a counting experiment in 40 equally spaced log(time) bins of gluino and mchamp lifetime hypotheses from 100 ns to 10^6s. Table 4 shows the results of the counting experiment for different lifetimes, for representative gluino and mchamp masses. For lifetimes shorter than one LHC orbit of 89 μs, we search within a time-window of 1.3 times the stopped particle's lifetime, to avoid the addition of backgrounds for time intervals during which the signal will have already decayed to unobservable levels. Thus, for lifetimes smaller than one orbit, both the number of observed events and the expected background depend on the time-window considered, which is a fraction of the total trigger livetime. Similarly, the effective luminosity is reduced for short lifetimes. However, for lifetimes larger than a single orbit, the trigger livetime, the expected background, and the number of observed events are independent of the lifetime. The effective luminosity decreases with lifetime for lifetimes longer than one LHC orbit, and the analysis sensitivity degrades with lifetimes longer than one LHC fill, since we do not consider signal that was produced in previous fills.

The data show no excess over background, and we set upper limits on the signal production cross section using a hybrid CL_S method [51, 52] to incorporate the systematic uncertainties [53] and a Tevatron-like ratio of profiled likelihoods as the test-statistic [54]. The 95% confidence level (CL) limits on the cross section times branching fraction (BF) as a function of lifetime for 1000 GeV gluinos and 1000 GeV mchamps are shown in Fig. 10 for combined 2015 and 2016 data. The detection sensitivity and the cross section limit are degraded for very small lifetimes, since any muons detected within two bunch crossings are vetoed. The limit curve is then flat for lifetimes greater than one orbit, since the numbers of observed and background events are constant. Finally, the sensitivity and effective luminosity are degraded for lifetimes larger than an LHC fill.

The combined 2015 and 2016 95% CL limits on the gluino and mchamp production cross sections times BF as a function of mass are shown in Fig. 11, for lifetimes between 10 μs and 1000 s, assuming 100% BF. We exclude gluino masses between 400 and 970 (970) GeV observed (ex-

Table 4: Counting experiment results for different lifetimes, for 2016 data.

Lifetime [s]	Effective Luminosity [fb^{-1}]	Trigger Livetime [hr]	Expected Background	Observed Events
10^{-7}	1.27	68	0.06 ± 0.00 (stat)$\pm$ 0.05 (syst)	0
10^{-6}	9.95	422	$0.36 \pm 0.01 \pm 0.29$	0
10^{-5}	13.34	581	$0.49 \pm 0.02 \pm 0.39$	0
10^{-4}	13.67	589	$0.50 \pm 0.02 \pm 0.40$	0
1	13.67	589	$0.50 \pm 0.02 \pm 0.40$	0
10^{3}	13.55	589	$0.50 \pm 0.02 \pm 0.40$	0
10^{4}	11.75	589	$0.50 \pm 0.02 \pm 0.40$	0
10^{5}	8.26	589	$0.50 \pm 0.02 \pm 0.40$	0
10^{6}	5.61	589	$0.50 \pm 0.02 \pm 0.40$	0

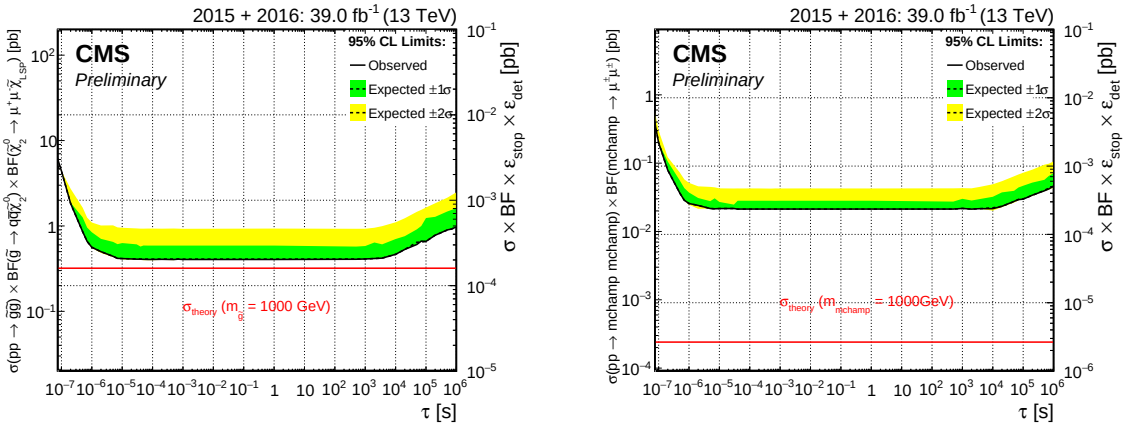

Figure 10: 95% CL cross section times BF limits on 1000 GeV gluino (left) and 1000 GeV mchamp (right) pair production as a function of lifetime, for combined 2015 and 2016 data. The observed limits are shown in the solid black line, the expected limits are shown in the dotted black line, the expected 1σ and 2σ bands are shown in green and yellow, respectively, and the theoretical cross sections assuming 100% BF are shown in the red line.

pected) and mchamp masses between 100 and 410 (410) GeV observed (expected) for lifetimes between 10 μs and 1000 s.

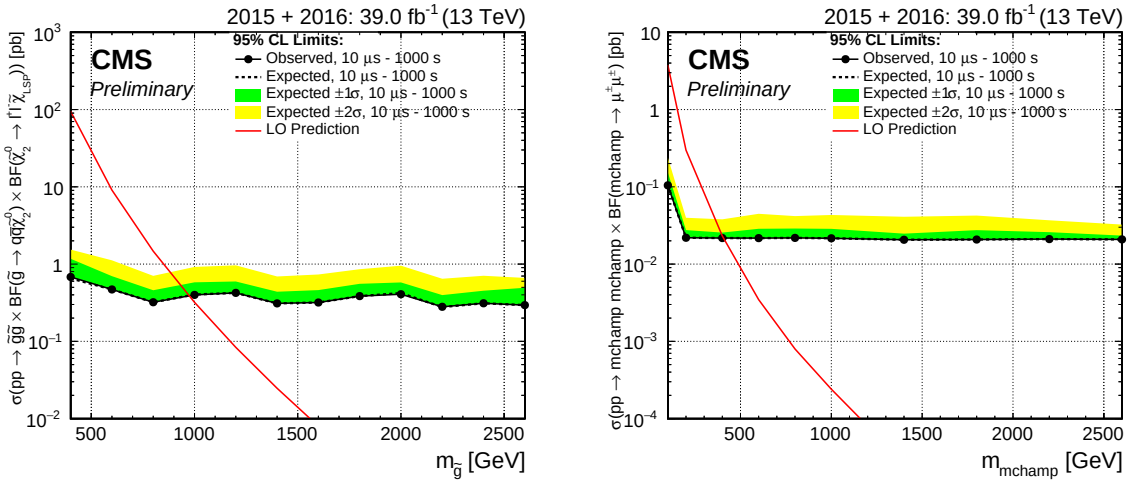

Figure 11: 95% CL cross section times BF limits on gluino (left) and mchamp (right) pair production as a function of mass, for lifetimes between 10 μs and 1000 s, for combined 2015 and 2016 data. The observed limits are shown in the solid black points, the expected limits are shown in the dotted black line, the expected 1σ and 2σ bands are shown in green and yellow, respectively, and the theoretical cross sections assuming 100% BF are shown in the red line.

9 Summary

A search for delayed muons produced in pp collisions at $\sqrt{s} = 13$ TeV has been performed at CMS with 2.8 fb^{-1} and 36.2 fb^{-1} data collected in 2015 and 2016. This search looked for new long-lived particles that stopped in the CMS detector and subsequently decayed to muons. These stopped particles were looked for when there were no collisions in the detector, namely, during gaps between LHC beam crossings.

No evidence of signal was found and 95% confidence level cross section times branching frac-

tion (BF) upper limits were set for combined 2015 and 2016 data. For lifetimes between 10 μs and 1000 s, limits were set between 1 and 0.01 pb for gluinos of mass between 400 and 2600 GeV and for mchamps of mass between 100 and 2600 GeV. Assuming a 100% BF, then for lifetimes between 10 μs and 1000 s, gluinos with mass between 400 and 970 (970) GeV observed (expected) are excluded, while mchamps with mass between 100 and 410 (410) GeV observed (expected) are excluded.

Cross section times BF limits were also set for each gluino and mchamp mass as a function of lifetime, for lifetimes between 100 ns and 10 days. These are the first limits for stopped particles that decay to muons at the LHC.

References

[1] S. Dimopoulos, M. Dine, S. Raby, and S. Thomas, "Experimental signatures of low energy gauge-mediated supersymmetry breaking", *Phys. Rev. Lett.* **76** (1996) 3494, doi:10.1103/PhysRevLett.76.3494.

[2] H. Baer, K. Cheung, and J. Gunion, "A heavy gluino as the lightest supersymmetric particle", *Phys. Rev. D* **59** (1999) 075002, doi:10.1103/PhysRevD.59.075002.

[3] T. Jittoh, J. Sato, T. Shimomura, and M. Yamanaka, "Long life stau in the minimal supersymmetric standard model", *Phys. Rev. D* **73** (2006) 055009, doi:10.1103/PhysRevD.73.055009.

[4] M. Strassler and K. Zurek, "Echoes of a hidden valley at hadron colliders", *Phys. Lett. B* **651** (2007) 374, doi:10.1016/j.physletb.2007.06.055.

[5] A. Arvanitaki et al., "Astrophysical probes of unification", *Phys. Rev. D* **79** (2009) 105022, doi:10.1103/PhysRevD.79.105022.

[6] N. Arkani-Hamed and S. Dimopoulos, "Supersymmetric unification without low energy supersymmetry and signatures for fine-tuning at the LHC", *JHEP* **06** (2005) 073, doi:10.1088/1126-6708/2005/06/073.

[7] K. Kohri and T. Takahashi, "Cosmology with long-lived charged massive particles", *Phys. Lett. B* **682** (2010) 337–341, doi:10.1016/j.physletb.2009.11.051.

[8] M. Byrne, C. Kolda, and P. Regan, "Bounds on charged, stable superpartners from cosmic ray production", *Phys. Rev. D* **66** (2002) 075007, doi:10.1103/PhysRevD.66.075007.

[9] P. Smith et al., "A search for anomalous hydrogen in enriched D2O, using a time-of-flight spectrometer", *Nucl. Phys. B* **206** (1982), no. 3, 333 – 348, doi:10.1016/0550-3213(82)90271-1.

[10] Particle Data Group, "Review of Particle Physics", *Chin. Phys.C* **40** (2016) 100001, doi:10.1088/1674-1137/40/10/100001.

[11] M. Fairbairn et al., "Stable massive particles at colliders", *Phys. Rept.* **438** (2007) 1–63, doi:10.1016/j.physrep.2006.10.002.

[12] P. Fayet, "Spontaneously broken supersymmetric theories of weak, electromagnetic and strong interactions", *Phys. Lett. B* **69** (1977) 489 – 494, doi:http://dx.doi.org/10.1016/0370-2693(77)90852-8.

[13] P. Fayet, "Massive gluinos", *Phys. Lett. B* **78** (1978) 417 – 420, doi:http://dx.doi.org/10.1016/0370-2693(78)90474-4.

[14] G. R. Farrar and P. Fayet, "Phenomenology of the production, decay, and detection of new hadronic states associated with supersymmetry", *Phys. Lett. B* **76** (1978) 575 – 579, doi:http://dx.doi.org/10.1016/0370-2693(78)90858-4.

[15] A. Arvanitaki et al., "Stopping gluinos", *Phys. Rev. D* **76** (2007) 055007, doi:10.1103/PhysRevD.76.055007.

[16] P. W. Graham, K. Howe, S. Rajendran, and D. Stolarski, "New measurements with stopped particles at the LHC", *Phys. Rev. D* **86** (2012) 034020, doi:10.1103/PhysRevD.86.034020.

[17] ATLAS Collaboration, "Search for long-lived stopped R-hadrons decaying out-of-time with pp collisions using the ATLAS detector", *Phys. Rev. D* **88** (2013) 112003, doi:10.1103/PhysRevD.88.112003.

[18] ATLAS Collaboration, "Search for decays of stopped, long-lived particles from 7 TeV pp collisions with the ATLAS detector", *Eur. Phys. J. C* **72** (2012) 1–21, doi:10.1140/epjc/s10052-012-1965-6.

[19] CMS Collaboration, "Search for decays of stopped long-lived particles produced in proton-proton collisions at $\sqrt{s} = 8\,\text{TeV}$", *Eur. Phys. J. C* **75** (2015) 151, doi:10.1140/epjc/s10052-015-3367-z.

[20] CMS Collaboration, "Search for Stopped Gluinos in pp Collisions at $\sqrt{s} = 7$ TeV", *Phys. Rev. Lett.* **106** (2011) 011801, doi:10.1103/PhysRevLett.106.011801.

[21] ATLAS Collaboration, "Search for heavy long-lived charged particles with the ATLAS detector in pp collisions at $\sqrt{s} = 7$ TeV", *Phys. Lett. B* **703** (2011) 428–446, doi:10.1016/j.physletb.2011.08.042.

[22] ATLAS Collaboration, "Search for stable hadronising squarks and gluinos with the ATLAS experiment at the LHC", *Phys. Lett. B* **701** (2011) 1–19, doi:10.1016/j.physletb.2011.05.010.

[23] ATLAS Collaboration, "Search for massive long-lived highly ionising particles with the ATLAS detector at the LHC", *Phys. Lett. B* **698** (2011) 353–370, doi:10.1016/j.physletb.2011.03.033.

[24] ATLAS Collaboration, "Searches for heavy long-lived sleptons and R-hadrons with the ATLAS detector in pp collisions at $\sqrt{s} = 7$ TeV", *Phys. Lett. B* **720** (2013) 277 – 308, doi:http://dx.doi.org/10.1016/j.physletb.2013.02.015.

[25] ATLAS Collaboration, "Search for long-lived, multi-charged particles in pp collisions at $\sqrt{s} = 7$ TeV using the ATLAS detector", *Phys. Lett. B* **722** (2013) 305 – 323, doi:doi:10.1016/j.physletb.2013.04.036.

[26] ATLAS Collaboration, "Search for heavy long-lived multi-charged particles in pp collisions at $\sqrt{s} = 8$TeV using the ATLAS detector", *Eur. Phys. J. C* **75** (2015) 362, doi:10.1140/epjc/s10052-015-3534-2.

[27] ATLAS Collaboration, "Search for metastable heavy charged particles with large ionisation energy loss in pp collisions at $\sqrt{s} = 8$TeV using the ATLAS experiment", *Eur. Phys. J. C* **75** (2015) 407, doi:10.1140/epjc/s10052-015-3609-0.

[28] CMS Collaboration, "Searches for long-lived charged particles in pp collisions at $\sqrt{s} = 7$ and 8 TeV", *JHEP* **07** (2013) 122, doi:doi:10.1007/JHEP07(2013)122.

[29] CMS Collaboration, "Search for heavy stable charged particles in pp collisions at $\sqrt{s} = 7$ TeV", *JHEP* **2011** (2011), no. 3, 24, doi:10.1007/JHEP03(2011)024.

[30] CMS Collaboration, "Search for fractionally charged particles in pp collisions at $\sqrt{s} = 7$ TeV", *Phys. Rev. D* **87** (2013) 092008, doi:10.1103/PhysRevD.87.092008.

[31] CMS Collaboration, "Search for heavy long-lived charged particles in pp collisions at $\sqrt{s} = 7$ TeV", *Phys. Lett. B* **713** (2012) 408–433, doi:10.1016/j.physletb.2012.06.023.

[32] CMS Collaboration, "Constraints on the pMSSM, AMSB model and on other models from the search for long-lived charged particles in proton-proton collisions at $sqrt(s) = 8$ TeV", *Eur. Phys. J. C* **75** (2015) 325, doi:10.1140/epjc/s10052-015-3533-3.

[33] LHCb Collaboration, "Search for long-lived heavy charged particles using a ring imaging Cherenkov technique at LHCb", (2015). arXiv:1506.09173.

[34] CMS Collaboration, "Search for long-lived charged particles in proton-proton collisions at $\sqrt{s} = 13$ TeV", *Phys. Rev. D* **94** (Dec, 2016) 112004, doi:10.1103/PhysRevD.94.112004.

[35] CMS Collaboration, "Search for heavy stable charged particles with 12.9 fb^{-1} of 2016 data", Technical Report CMS-PAS-EXO-16-036, CERN, Geneva, 2016.

[36] CMS Collaboration, "The CMS experiment at the CERN LHC", *JINST* **3** (2008) S08004, doi:10.1088/1748-0221/3/08/S08004.

[37] G. Giudice and A. Romanino, "Split supersymmetry", *Nucl. Phys. B* **699** (2004) 65, doi:http://dx.doi.org/10.1016/j.nuclphysb.2004.11.048.

[38] N. Arkani-Hamed and S. Dimopoulos, "Supersymmetric unification without low energy supersymmetry and signatures for fine-tuning at the LHC", *JHEP* **2005** (2005) 073, doi:10.1088/1126-6708/2005/06/073.

[39] CMS Collaboration, "Interpretation of searches for supersymmetry with simplified models", *Phys. Rev. D* **88** (Sep, 2013) 052017, doi:10.1103/PhysRevD.88.052017.

[40] G. L. Kane, C. Kolda, L. Roszkowski, and J. D. Wells, "Study of constrained minimal supersymmetry", *Phys. Rev. D* **49** (Jun, 1994) 6173–6210, doi:10.1103/PhysRevD.49.6173.

[41] A. H. Chamseddine, R. Arnowitt, and P. Nath, "Locally Supersymmetric Grand Unification", *Phys. Rev. Lett.* **49** (Oct, 1982) 970–974, doi:10.1103/PhysRevLett.49.970.

[42] P. Langacker and G. Steigman, "Requiem for a fractionally charged, massive particle", *Phys. Rev. D* **84** (2011) 065040, doi:10.1103/PhysRevD.84.065040.

[43] C. S. Aulakh, K. Benakli, and G. Senjanovic, "Reconciling High-Scale Left-Right Symmetry with Supersymmetry", *Phys. Rev. Lett.* **79** (1997) 2188–2191, doi:10.1103/PhysRevLett.79.2188.

[44] T. Sjöstrand, S. Mrenna, and P. Skands, "PYTHIA 6.4 Physics and manual", *JHEP* **2006** (2006), no. 05, 026, doi:10.1088/1126-6708/2006/05/026.

[45] T. Sjöstrand, S. Mrenna, and P. Skands, "A brief introduction to PYTHIA 8.1", *Comput. Phys. Commun.* **178** (2008), no. 05, 852 – 867, doi:http://dx.doi.org/10.1016/j.cpc.2008.01.036.

[46] GEANT4 Collaboration, "Geant4: A simulation toolkit", *Nucl. Instrum. Methods A* **506** (2003) 250 – 303, doi:http://dx.doi.org/10.1016/S0168-9002(03)01368-8.

[47] GEANT4 Collaboration, "Geant4 developments and applications", *IEEE Trans. Nucl. Sci.* **53** (2006) 270 – 278, doi:10.1109/TNS.2006.869826.

[48] CMS Collaboration, "Muon Reconstruction and Identification Improvements for Run-2 and First Results with 2015 Run Data", CMS Detector Performance Summaries 2015/015, 2015.

[49] CMS Collaboration, "CMS Luminosity Measurement for the 2015 Data Taking Period", *CMS Public Analysis Note* **CMS-PAS-LUM-15-001** (2015).

[50] CMS Collaboration, "CMS Luminosity Measurements for the 2016 Data Taking Period", Technical Report CMS-PAS-LUM-17-001, CERN, Geneva, 2017.

[51] T. Junk, "Confidence level computation for combining searches with small statistics", *Nucl. Instrum. Methods A* **434** (1999) 435 – 443, doi:http://dx.doi.org/10.1016/S0168-9002(99)00498-2.

[52] A. L. Read, "Presentation of search results: the CL s technique", *J Phys G* **28** (2002) 2693, doi:10.1088/0954-3899/28/10/313.

[53] R. Cousins and V. Highland, "Incorporating systematic uncertainties into an upper limit", *Nucl. Instrum. Methods A* **320** (1992) 331, doi:10.1016/0168-9002(92)90794-5.

[54] The ATLAS Collaboration, The CMS Collaboration, The LHC Higgs Combination Group Collaboration, "Procedure for the LHC Higgs boson search combination in Summer 2011", Technical Report CMS-NOTE-2011-005. ATL-PHYS-PUB-2011-11, CERN, Geneva, Aug, 2011.